

Article

Characterization of a Contaminated Site Using Hydro-Geophysical Methods: From Large-Scale ERT Surface Investigations to Detailed ERT and GPR Cross-Hole Monitoring

Mirko Pavoni ^{1,*}, Jacopo Boaga ¹ , Luca Peruzzo ¹, Iliaria Barone ¹ , Benjamin Mary ² and Giorgio Cassiani ¹ 

¹ Department of Geosciences, University of Padova, 35100 Padova, Italy; luca.peruzzo.1@unipd.it (L.P.); ilaria.barone@unipd.it (I.B.); giorgio.cassiani@unipd.it (G.C.)

² Tec4Agro Group, Institute of Agricultural Sciences—CSIC, 28006 Madrid, Spain; benjamin.mary@ica.csic.es

* Correspondence: mirko.pavoni@unipd.it

Abstract: This work presents the results of an advanced geophysical characterization of a contaminated site, where a correct understanding of the dynamics in the unsaturated zone is fundamental to evaluate the effective management of the remediation strategies. Large-scale surface electrical resistivity tomography (ERT) was used to perform a preliminary assessment of the structure in a thick unsaturated zone and to detect the presence of a thin layer of clay supporting an overlying thin perched aquifer. Discontinuities in this clay layer have an enormous impact on the infiltration processes of both water and solutes, including contaminants. In the case here presented, the technical strategy is to interrupt the continuity of the clay layer upstream of the investigated site in order to prevent most of the subsurface water flow from reaching the contaminated area. Therefore, a deep trench was dug upstream of the site and, in order to evaluate the effectiveness of this approach in facilitating water infiltration into the underlying aquifer, a forced infiltration experiment was carried out and monitored using ERT and ground-penetrating radar (GPR) measurements in a cross-hole time-lapse configuration. The results of the forced infiltration experiment are presented here, with a particular emphasis on the contribution of hydro-geophysical methods to the general understanding of the subsurface water dynamics at this complex site.

Keywords: hydrogeophysics; contaminated site; infiltration experiment; time-lapse geophysics; ERT; GPR



Citation: Pavoni, M.; Boaga, J.; Peruzzo, L.; Barone, I.; Mary, B.; Cassiani, G. Characterization of a Contaminated Site Using Hydro-Geophysical Methods: From Large-Scale ERT Surface Investigations to Detailed ERT and GPR Cross-Hole Monitoring. *Water* **2024**, *16*, 1280. <https://doi.org/10.3390/w16091280>

Academic Editor: Juan José Durán

Received: 20 March 2024

Revised: 22 April 2024

Accepted: 24 April 2024

Published: 29 April 2024



Copyright: © 2024 by the authors. Licensee MDPI, Basel, Switzerland. This article is an open access article distributed under the terms and conditions of the Creative Commons Attribution (CC BY) license (<https://creativecommons.org/licenses/by/4.0/>).

1. Introduction

In the characterization of contaminated sites, direct drilling methods and geochemical analysis of groundwater may not be completely representative of the entire investigated area, leaving some uncertainties in the management of remediation and secure strategies [1]. Therefore, utilizing near-surface geophysical techniques is a relatively fast and economical approach to retrieve further information about the structure of the subsurface and the hydrological dynamics [2], particularly in terms of the extensive spatial coverage and refined sampling that geophysics can provide. Among the different geophysical methods, electrical resistivity tomography (ERT) and ground-penetrating radar (GPR) are widely used for the characterization of contaminated sites [3,4], since electrical and dielectric properties are closely related to the lithology, soil texture and particularly to the water content, water quality and the presence of non-aqueous-phase contaminant liquids [5,6].

In this work, we present the main results of an extensive geophysical survey campaign conducted at a contaminated site in the Friuli High Plain, north-eastern Italy. The presence of contaminants in groundwater was detected around a former industrial site. The geological conditions of the site can be described as a relatively simple stratigraphic sequence composed of an upper unsaturated gravel layer, housing also a perched aquifer, discontinuously interrupted by a thin layer of clay (a paleo-soil) at a 6–7 m depth. Below

the clay layer, another thick unsaturated gravelly zone reaches a depth of about 100 m, where the water table of the regional main aquifer is located. Thus, the development and consistency of the clay layer are critical from a hydraulic point of view in order to prevent deeper infiltration of pollution from the surface [7]. In the investigated area, to prevent the subsurface flow from reaching the contaminated site, it was planned to force the water infiltration into the deeper underlying thick unsaturated zone and the deep aquifer by interrupting the continuity of the clay layer with a draining trench upstream of the industrial site.

Firstly, to define the most suitable position for the trench, large-scale surface ERT surveys were performed to map the extension and continuity of the clay layer around and within the industrial site. Once the optimal position was defined, ERT cross-borehole investigations were performed before and after the realization of a pilot stretch of the draining trench to evaluate the effects of excavation. Finally, to verify the effectiveness of the trench in draining the shallow subsurface water flow into the deeper aquifer, two forced infiltration experiments were carried out and monitored using both ERT and GPR cross-borehole measurements in time-lapse configuration [8–10].

Preliminary synthetic models, based on a priori geological information, were tested in order to optimize the data acquisition strategies. In particular, we tested different ERT survey strategies (with different electrode array lengths, spacings and configurations) against different possible geological models, varying the thickness and depth of the conductive clay layer.

The goal of this work is to demonstrate the effectiveness of the use of geophysical investigations in the overall strategy of characterization and remediation of contaminated sites. In order to fully benefit from its information content, geophysics must be carefully planned, both for characterization and monitoring (time-lapse) modes, often with the support of synthetic experiments in the planning stage.

2. Site Description

2.1. Geological Framework

The investigation site is located in a High Plain of north-eastern Italy. This is the easternmost portion of the foreland area of the alpine chain, and the plain is a consequence of the progressive accumulation of fluvio-glacial sediments. During the last glacial maximum (LGM), the glacial and periglacial conditions in the mountain basins promoted a considerable production of sediments, and the development of the glaciers down to the valley outlets guaranteed efficient transport, feeding large fluvio-glacial systems. In this Eastern High Plain, this high sedimentation rate promoted the development of large river systems (e.g., the Isonzo, Torre, Tagliamento, Cellina, and Meduna rivers), and consequently the formation of extensive alluvial megafans, i.e., a fan-shaped depositional system with an extension that can exceed thousands of km², characterized by an apical portion consisting of gravelly deposits, and a distal portion essentially composed of fine sediments [11]. In the High Plain, the subsoil is mainly composed of alluvial deposits of braided systems that continuously migrated due to periodical avulsions. Therefore, in the evolution of the megafans, coarse sedimentation phases alternated with destructive and steady-state moments, even prolonged, which ensured the formation of soils that may have been subsequently buried (paleosoils) [12]. Finally, during the Holocene, glacier retreat led to a decrease in the sedimentation rate, the confinement of rivers within incised channels, and the transition of large areas of megafans into bypass surfaces without deposition. In these areas, the gravels have been weathered, generating soils with clay layers [13].

2.2. Experimental Area

At the contaminated site, the subsoil is composed of the Vivaro Unit, i.e., gravels with a sub-horizontal coarse stratification, sometimes with a slightly silty–sandy matrix, in which buried paleo-soils are interspersed [14]. This stratigraphic structure is confirmed by the boreholes realized for ERT and GPR investigations. As shown in Figure 1a, a 20 m deep

perforation highlights the presence of a thick layer of gravel, which is cut by a thin level of clay at about a 7 m depth. Four such boreholes have been drilled and equipped with 24 electrodes each from a depth of 1.6 m to the bottom of the boreholes (0.8 m spacing). Figure 1b presents the geometry of the boreholes (red circles) and the pilot-scale draining trench. The latter has a length of approximately 17 m, a depth of 13 m (as shown in Figure 1c) and is about 1 m wide. After excavation it was completely filled with permeable coarse gravel. This stretch of trench was intended as a pilot test to confirm the effectiveness of the proposed intervention; the full trench was planned to have a length exceeding 100 m. This pilot trench was realized in correspondence with an ERT surface transect collected prior to the excavation. Four ERT-equipped boreholes were drilled on both sides of the trench, allowing for meaningful cross-hole acquisitions. Note that the boreholes also allow for cross-hole GPR acquisitions given the relatively small borehole distance (8 m).

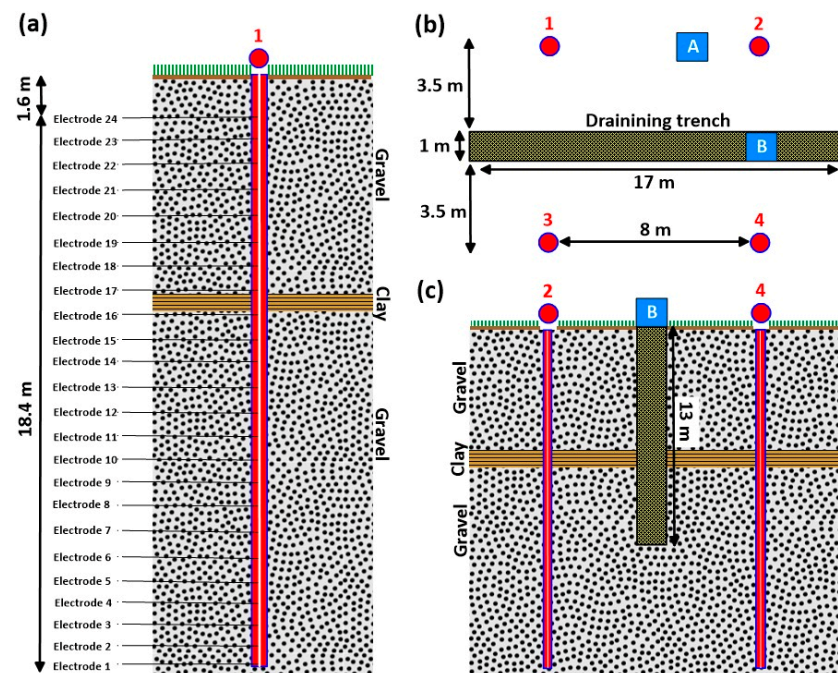


Figure 1. (a) Schematization of borehole 1 and the stratigraphy found during the drilling: 24 electrodes placed from the bottom of the borehole (20 m depth) to a 1.6 m depth; (b) planned geometry of the area with four boreholes (red dots), the draining trench (parallel to the ERT surface line), and the position of the water injections (blue square A–B); (c) vertical section of the area between borehole 2 and borehole 4, and the draining trench in between. Note that the thickness of the clay layer is in the 0.5 m range and less (considering all four drilled boreholes).

Two infiltration experiments were conducted in the pilot zone, with the purpose of assessing to what extent the dug trench, interrupting the continuity of the clay layer, was capable of conveying water into the deeper unsaturated zone, as expected. The first infiltration experiment (indicated by the blue square “A” in Figure 1b) was realized on the side of the trench, with the injection point located between borehole 1 and borehole 2. The second infiltration experiment (blue square “B” in Figure 1b,c) was realized by placing the water injection point right above the trench, between borehole 2 and borehole 4. In both cases, a square meter at the surface was isolated using wooden walls and a constant water flow rate into the box was ensured by a water tanker for a total injected volume of nearly 17 cubic meters.

3. Methods

3.1. Electrical Resistivity Tomography (ERT)

ERT surveys are performed with multi-electrode instruments to retrieve the electrical resistivity distribution of the subsurface. The measurements were carried out with an array of several dozens of electrodes, either placed at the ground surface (the most common arrangement) or in dedicated boreholes, and are galvanically coupled with the soil. The measurement consists of injecting an electrical current with two electrodes and recording the voltage difference that arise at other pairs of electrodes [5]. Based on the target of the survey, different types of acquisition schemes can be adopted; Wenner-alpha and Wenner-Schlumberger schemes (injection dipole outside the potentiometric one) guarantee a higher vertical resolution, while a dipole-dipole scheme (injection dipole is adjacent to the potentiometric one) allows for a higher lateral sensitivity (for details see [15]). The penetration depth of a measured point is linked to the length of the quadrupole; consequently, the maximum depth of investigation is defined by the total length of the electrode array. For the same reason, in cross-hole configuration, the distance between neighbouring boreholes cannot be too large, generally no larger than the depth of the boreholes themselves. On the other hand, the resolution of the investigation is linked to the spacing between the electrodes, and it is higher close to the electrodes [15]. Therefore, the resolution of ERT surface measurements decreases in depth. Consequently, when a high resolution at depth is required, cross-hole ERT with borehole electrodes can be adopted. Nevertheless, since the number of the electrodes controlled by a multi-electrode device is limited, usually ranging between 48 and 120 channels, it is necessary to find a compromise between the spacing and the length of the array, considering the requested resolution of the survey (e.g., the spacing should not be larger than the thickness of the layers) and its penetration (about $\frac{1}{4}$ of the total length of the array) [5].

The quality of ERT datasets can be evaluated by a combination of two approaches: (i) stacking errors, where each quadrupole is measured several times and a standard deviation is calculated for each one and (ii) reciprocal errors, where for each quadrupole, the measurement is performed by exchanging the injection dipole and the potentiometric dipole, and the difference between direct and reciprocal measurements is calculated for each quadrupole [16]. Finally, since the measurements are influenced by the contribution of different materials that compose the subsurface, the acquired ERT datasets need to be inverted to identify the most suitable subsurface resistivity model that reproduces the measurements [17].

3.1.1. ERT Forward Modelling

Starting from a known subsoil structure with a defined resistivity distribution, and an array of electrodes at the surface, we can discretize the investigated domain with a mesh and numerically calculate, by applying Poisson's equation (for details, see [15]), the voltages that arise at the electrodes of the array if we inject the electrical current i with a dipole A-B. Therefore, we can find the potential difference ΔV for any pair of potentiometric dipoles M-N of the array and obtain a synthetic dataset of apparent resistivities ρ_a by applying Equation (1), which applies to surface electrode configurations only. This process is called the "forward problem" or "forward modelling".

$$\rho_a = \frac{\Delta V}{i} 2\pi \left(\frac{1}{AM} - \frac{1}{BM} - \frac{1}{AN} + \frac{1}{BN} \right)^{-1} = \frac{\Delta V}{i} K \quad (1)$$

Here, K is the geometric factor of the measured quadrupole. In borehole measurements, the electric current is flowing in all directions. Consequently, K needs to be recalculated, as shown in Equation (2) (where z is the depth of the electrodes):

$$K = 4\pi \left[\left(\frac{1}{|z_A - z_M|} + \frac{1}{z_A + z_M} \right) - \left(\frac{1}{|z_B - z_M|} + \frac{1}{z_B + z_M} \right) - \left(\frac{1}{|z_A - z_N|} + \frac{1}{z_A + z_N} \right) + \left(\frac{1}{|z_B - z_N|} + \frac{1}{z_B + z_N} \right) \right]^{-1} \quad (2)$$

Once a synthetic dataset is computed, an inversion framework can be applied to the calculated apparent resistivities to obtain an inverted synthetic resistivity model.

In the presented work, the Python-based software ResIPy (v3.4.2) [16] was used to perform the forward modelling process and define the optimal acquisition parameters for the preliminary ERT surface measurements. Based on geological information, we created different subsurface models, as shown in Figure 2. In each model, an upper (relatively) high resistive layer of $300 \Omega\text{m}$ represents a weathered gravel with a slightly silty–sandy matrix, which is cut by a low resistive layer (i.e., clay) of $10 \Omega\text{m}$ at a 5 m depth in Figure 2a,b and at a 10 m depth in Figure 2c,d. In the models of Figure 2a,c, the low resistive layer has a thickness of 0.50 m, while in the models of Figure 2b,d, the thickness is 2 m. In all models, the bottom layer of $450 \Omega\text{m}$ represents the deeper, unsaturated silty gravel layer.

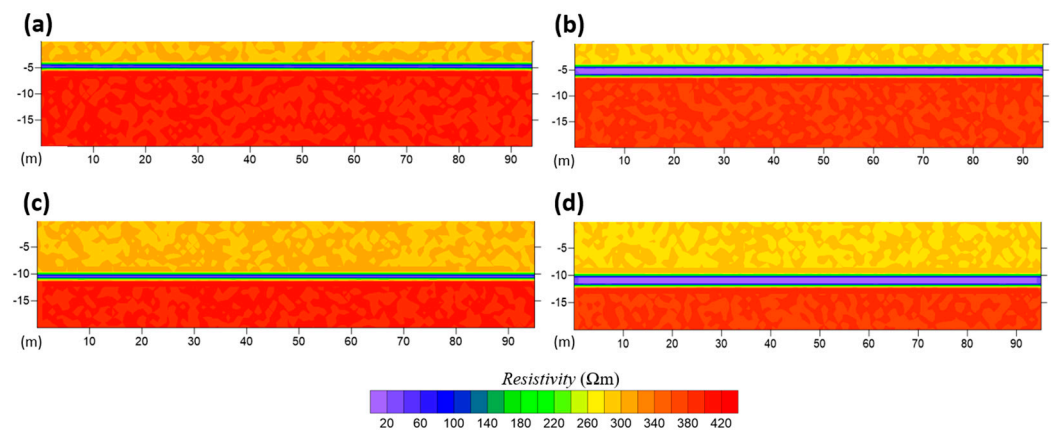


Figure 2. The subsurface models used for ERT surface forward modelling. In each model, an upper high resistive layer of $300 \Omega\text{m}$ is cut by a low resistive layer of $10 \Omega\text{m}$ at 5 m of depth in (a,b), at 10 m of depth in (c,d). In the models of (a,c), the low resistive layer has a thickness of 0.50 m, while in the models of (b,d) the thickness is 2 m.

Firstly, forward modelling was performed considering a surface ERT investigation with different electrode spacings: a dipole–dipole acquisition scheme and testing different values of skip (i.e., the number of electrodes skipped to create a dipole).

Afterwards, the same subsurface structure was used to perform a cross-borehole ERT survey. As shown in Figure 3, we considered a low-resistive layer with both a thickness of 0.50 m (Figure 3a–c) and 2 m (Figure 3d–f) at a depth of 5 m. We tested boreholes with different electrode spacings (0.5 m in Figure 3a,b,d,e, and 1 m in Figure 3c,f), a skip 4 AB-MN configuration (injection dipole electrodes in the same borehole, and potentiometric dipole electrodes in the other borehole), and different borehole separations (5 m in Figure 3a,d, and 8 m Figure 3b,c,e,f).

3.1.2. ERT Inverse Modelling

Inverse modelling is used to calculate the most reliable resistivity model that can reproduce the measured apparent resistivities within data error bounds. This is an iterative process where forward models are calculated repeatedly in order to minimize the misfit between the predicted and observed data [17]. However, different resistivity models can lead to practically the same response—within data error levels—and a unique solution can be found by formulating the inversion process as a regularized optimization problem, applying Occam’s approach [18], which searches for the smoothest model that can fit the measured data within their error level (for details, see [15]).

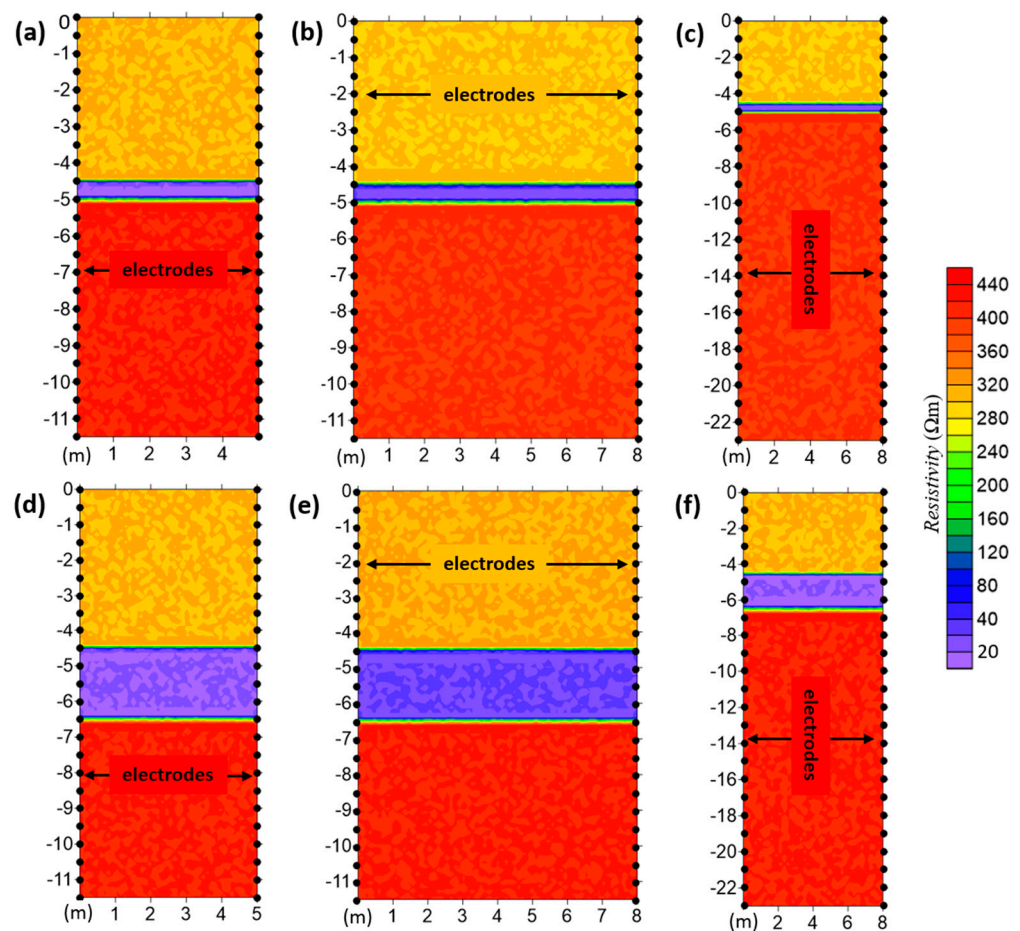


Figure 3. The subsurface models used to perform the ERT cross-borehole forward modelling process. In each model, an upper high resistive layer of $300 \Omega\text{m}$ is cut by a low resistive layer of $10 \Omega\text{m}$ at 5 m of depth in (a,b), at 10 m of depth in (c,d). In the models of (a–c), the low resistive layer has a thickness of 0.50 m, while in the models of (d–f) the thickness is 2 m.

Defining an optimal error degree for the inversion process is a key factor to avoid unrealistic artifacts in the final inverted resistivity model [5]. The expected data error can be estimated by using the stacking error, but usually this approach overestimates the data quality and a better assessment of the error can be achieved by considering reciprocal measurements [19]. Once a reciprocal error threshold value is defined, all the quadrupoles with higher values are filtered out and not considered during the inversion process. High-quality ERT datasets have reciprocal errors of lower than 5%, while low-quality datasets have values as high as 20%, typically when the galvanic contact between electrodes and the ground surface is poor [20].

In this work, inverse modelling of the acquired datasets was performed using the Python-based software ResIPy [16] and, for each dataset, we defined a boundary threshold for the reciprocal error that allowed for a reliable quality of the measured apparent resistivities but at the same time a homogeneous distribution of measured points in the pseudo-section [21,22]. For the surface ERT measurements, an expected data error of 10% was defined, while for the ERT cross-borehole datasets, we selected a more comfortable 5% error level. All inverted models presented here have a final RMS (Root Mean Square—evaluation of the normalized misfit between calculated and measured data) close to 1.

3.1.3. ERT Time-Lapse Survey

ERT surveys can also be used to monitor time-dependent subsurface processes through changes in resistivity over time. This kind of investigation is particularly useful to monitor natural processes in the subsoil (e.g., moisture variation during the year [23,24] or as a consequence of forced irrigation experiments, with several hundreds or thousands of litres of water injected into the subsurface [10,25]). In order to enhance the changes from one time frame to the next, ratio or difference inversion approaches are usually applied [5]. For each quadrupole in the dataset, the parameter to be inverted is the ratio or the difference between the resistance ($R = \Delta V/I$) measured in the considered time step and the initial resistance measured before the water injection.

Time-lapse inversion is a powerful approach to highlight small variations in resistivity that would otherwise be overwhelmed by error differences in subsequent absolute resistivity images [26]. For each time step, the results are consequently given in terms of resistivity variation with respect to the initial model obtained before the water injection. Therefore, after the inversion process, only the initial reference model will be plotted in terms of absolute resistivities, while the following time step results will be plotted in terms of variations in resistivity with respect to such an initial model.

In the presented work, two forced infiltration experiments were carried out and monitored with ERT cross-borehole time-lapse measurements, as well as repeated GPR measurements—as described below. In each survey, a representative value of reciprocal error was defined for the acquired ERT datasets, and only the common quadrupoles in all filtered datasets were used to perform the time-lapse ratio inversion.

3.1.4. ERT Data Acquisition

All ERT surveys (surface, cross-borehole, and time-lapse) were carried out using a Syscal Pro resistivimeter (Iris Instruments, Orléans, France), using a stacking range between 3 and 6 (5% standard deviation threshold), and with direct reciprocal measurements.

As previously discussed, several ERT surface investigation lines were collected around and within the contaminated area to evaluate the depth and continuity of the clay layer. In this work, we only focused on the survey line acquired upstream of the industrial site, in correspondence with the area chosen for the realization of the draining trench and the boreholes. Based on the results of the previous forward modelling tests, surface ERT measurements were performed using an array of 120 electrodes spaced at 0.80 m and a dipole–dipole skip 8 acquisition scheme.

To evaluate the effectiveness of the trench, ERT cross-borehole measurements were collected before and after the pilot trench excavation and backfilling with coarse permeable material. The datasets were acquired using 48 electrodes, with 24 in each borehole (see Figure 1), using an AB-MN skip 4 acquisition scheme. To better evaluate the resistivity variation linked to the excavation, a ratio inversion process was also applied to the data acquired before and after excavation in correspondence with the section between boreholes 1 and 3 (see Figure 1).

Two forced infiltration experiments were also performed using ERT cross-borehole time-lapse measurements (also using four electrodes in the surface between the boreholes) using an AB-MN skip 4 acquisition scheme. As shown in Figure 1b, the first experiment was performed between borehole 1 and borehole 2, while the second experiment was performed between borehole 2 and 4 (one week after the first experiment). In each experiment, a time-zero dataset was acquired in natural dry conditions; afterwards, about 16,600 litres of salt water were injected into the subsurface over 9 h, and twelve ERT measurements were acquired during the following 28 h (as shown in Table 1 for the first infiltration experiment—the same acquisition scheme was used for the second infiltration experiment).

Table 1. Time steps of the first forced infiltration experiment (between borehole 1 and 2—see blue square A in Figure 1b) monitored using ERT and GPR time-lapse measurements. The second infiltration experiment was realized with the same acquisition parameters and time steps (one week after the first experiment).

Time	ERT Time Step	Water Released
11:00	t0	-
12:00	-	Start
12:35	t1	1000 L
13:08	t2	2000 L
13:45	t3	3000 L
14:20	t4	4000 L
14:55	t5	5000 L
15:30	t6	6000 L
16:00	t7	7000 L
21:30	-	16,600 L (End)
07:50 (+1 day)	t8	-
10:00 (+1 day)	t9	-
12:00 (+1 day)	t10	-
14:00 (+1 day)	t11	-
16:00 (+1 day)	t12	-

3.2. Ground-Penetrating Radar (GPR)

Spatiotemporal variations in water content in shallow soil layers can be efficiently estimated using techniques that measure the electrical permittivity ϵ or the relative electrical permittivity (also called the dielectric constant), ϵ_r , of porous media [27–30]. ϵ_r is strongly affected by the presence of water in soil pores, as the corresponding dielectric constant of water is so high that it overcomes any other solid or fluid component in the porous medium. GPR is particularly suitable to measure ϵ_r , as the propagation of electromagnetic waves, to a first approximation, can be directly related to the value of the bulk ϵ_r of the material:

$$\sqrt{\epsilon_r} = \frac{c}{v} \quad (3)$$

where c is the electromagnetic wave speed in the vacuum (0.3 m/ns) and v is the measured velocity of propagation of the radar waves. In order to measure GPR velocities, the transmitter probe must be separated from the receiver one (using a bi-static GPR), and the time of arrival of the GPR waves must be defined at a known distance between the two. This can be achieved on the surface or in the borehole. In the infiltration test zone of the study site, thanks to the drilled boreholes, which all have a plastic casing that does not impede the propagation of electromagnetic waves outside the boreholes, we could exploit the same boreholes and equip them with ERT electrodes to acquire cross-hole GPR data. For this purpose, we used a Pulse-Ekko 100 MHz antenna system. Both the ZOP (zero offset profile, e.g., [31]) and MOG (multi-offset gather, e.g., [32,33]) were tested. In this case, VRP (vertical radar profiling [34]) had an unfavourable geometry and was not tested. In the ZOP configuration, the receiver and transmitter antennas go down at the same time along the boreholes, thus keeping the distance between the two probes, i.e., the distance between the two boreholes, fixed. In the MOG configuration, the transmitter antenna is moved in different positions independently from the receiver antenna, collecting a much more detailed survey between the boreholes and allowing for a 2D tomographic reconstruction. Cross-hole GPR data were collected for 2 days before, during and after the second infiltration test using boreholes 2 and 4 for a total of 14 different datasets.

4. Results

4.1. ERT Forward Modelling Results

Figure 4 shows the inverted synthetic models derived from the forward modelling process applied to the subsurface structure of Figure 2a using surface ERT configurations.

The low-resistive layer of clay is in this case very thin (0.5 m) and is smeared into a much thicker, less-conductive layer in the results of Figure 4a, obtained by simulating an array of 96 electrodes with a 0.5 m electrode spacing and a dipole–dipole skip 0 acquisition scheme. This is completely consistent with the very well-known equivalence problem in classical geoelectrical acquisitions. In fact, albeit with different final results configurations, the same phenomenon manifests itself in all other configurations in Figure 4 and is the result of the thin, very conductive layer being able to short circuit the current coming from the surface through itself, effectively shielding any other structure lying below this layer [35]. Note that this phenomenon is linked to the continuity of the clay layer—should the layer have any sizeable discontinuity, the discontinuity would become visible and part of the underlying structure would also be revealed.

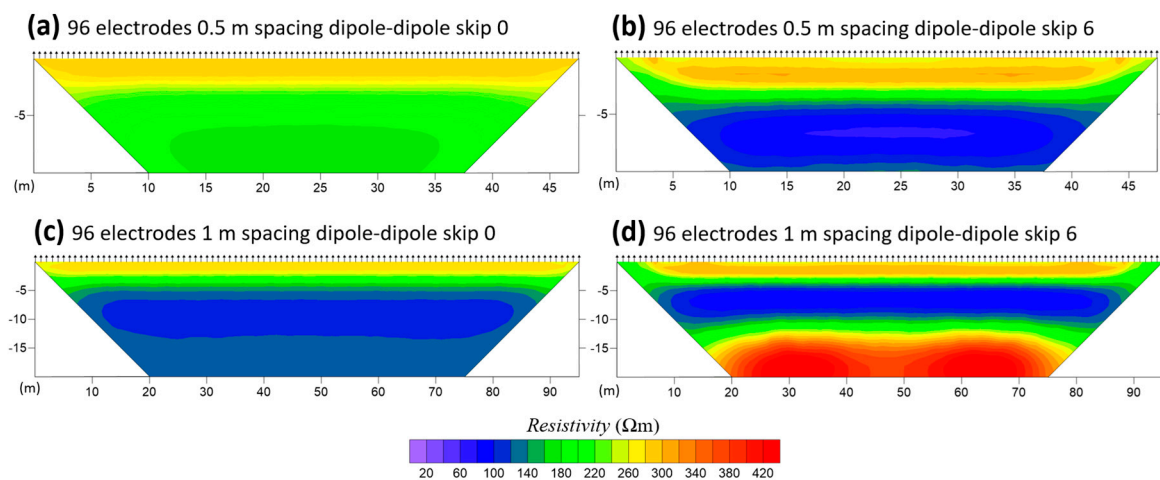


Figure 4. Inverted synthetic models obtained considering the subsurface model in Figure 2a. (a,b) show, respectively, the inverted synthetic models found with 96 electrodes, a 0.5 m spacing, and dipole–dipole skip 0 (a) and skip 6 (b) configurations; (c,d) show, respectively, the inverted synthetic models found with 96 electrodes, a 1 m spacing, and dipole–dipole skip 0 (c) and skip 6 (d) configurations.

Figure 5 presents the inverted synthetic models obtained from the forward modelling process applied to the subsurface structure of Figure 2b, with a 2 m-thick clay layer at a 5 m depth. The results are very similar to the ones in Figure 4, as the short-circuiting effect of the clay layer is the same, if not more pronounced.

Considering the clay layer at a 10 m depth (Figure 2c,d), and testing the same electrode array and acquisition schemes, Figure 6 shows again the limitation of surface ERT acquisitions in the face of a continuous conductive layer: its thickness cannot be ascertained and the structures below this layer remain unknown. Yet, this phenomenon is strictly linked to the continuity of this electrically conductive, hydraulically impeding layer. Thus, even though the overall deep structure of the subsoil cannot be imaged entirely, the continuity of the layer can be proven using surface ERT.

Figure 7 shows the inverted synthetic models considering an ERT cross-borehole configuration. Figure 7a–c present, respectively, the results obtained considering the subsurface structures and the electrode geometries in Figure 3a–c. In Figure 7a, with boreholes placed 5 m apart and an electrode spacing of 0.5 m, the inverted synthetic model correctly defines the subsurface structure, i.e., the depth, thickness and resistivity value of the clay layer. Given the geometry of the current injection, the short-circuiting phenomenon observed in surface acquisitions does not take place. Increasing the distance between the boreholes to 8 m, as shown in Figure 7b, leads to some uncertainties; i.e., the clay layer seems to have a larger thickness in the central area of the model, and a low resistivity area ($\sim 65 \Omega\text{m}$) is found close to the surface. These are effects of the loss in resolution away from the electrode areas, with the corresponding prevalence of the smoothing effect of Occam's

inversion. As shown in Figure 7c, modifying the electrode spacing to 1 m (considering a borehole separation of 8 m) allows for a reduction in these artifacts; i.e., the clay layer thickness is more homogeneously retrieved in the central area of the model. Considering a 2 m-thick clay layer, the configuration with a 5 m borehole separation and a 0.5 m electrode spacing, as shown in Figure 7d, correctly reproduces the subsurface structure in Figure 3d. Increasing the borehole separation to 8 m (considering a 0.5 m electrode spacing), as shown in Figure 7e, does not produce artifacts, and allows for the correct definition of the model of Figure 3e. A reliable inverted synthetic model is also found by increasing the electrode spacing to 1 m, as shown in Figure 7d.

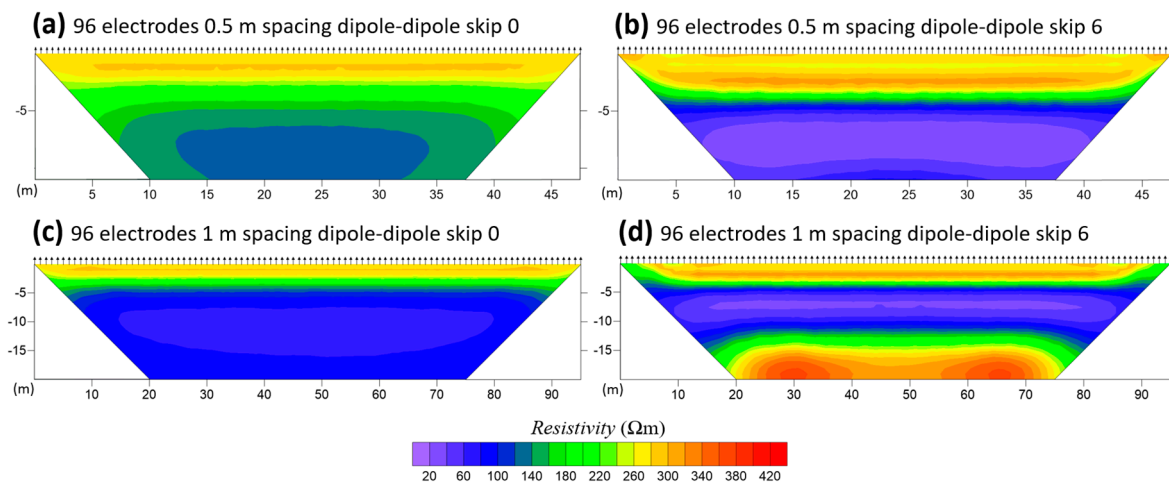


Figure 5. Inverted synthetic models obtained considering the subsurface model in Figure 2b. (a,b) show, respectively, the inverted synthetic models found with 96 electrodes, a 0.5 m spacing, and dipole–dipole skip 0 (a) and skip 6 (b) configurations; (c,d) show, respectively, the inverted synthetic models found with 96 electrodes, a 1 m spacing, and dipole–dipole skip 0 (c) and skip 6 (d) configurations.

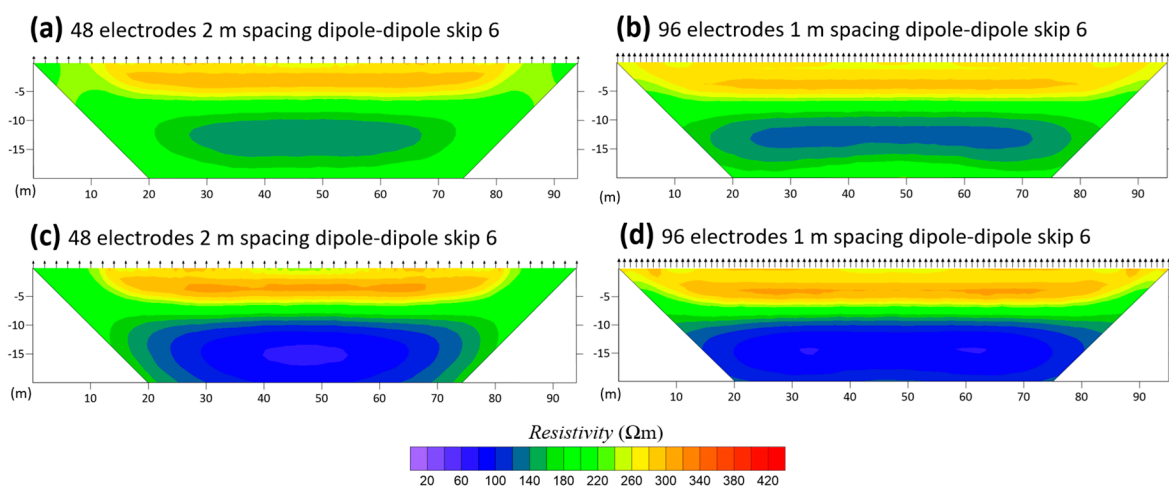


Figure 6. (a) shows the inverted synthetic model of Figure 2c found with 48 electrodes and a 2 m spacing; (b) shows the inverted synthetic model of Figure 2c found with 96 electrodes and a 1 m spacing; (c) shows the inverted synthetic model of Figure 2d found with 48 electrodes and a 2 m spacing; (d) shows the inverted synthetic model of Figure 2d found with 96 electrodes and a 1 m spacing. All the models were calculated using a dipole–dipole skip 6 acquisition scheme.

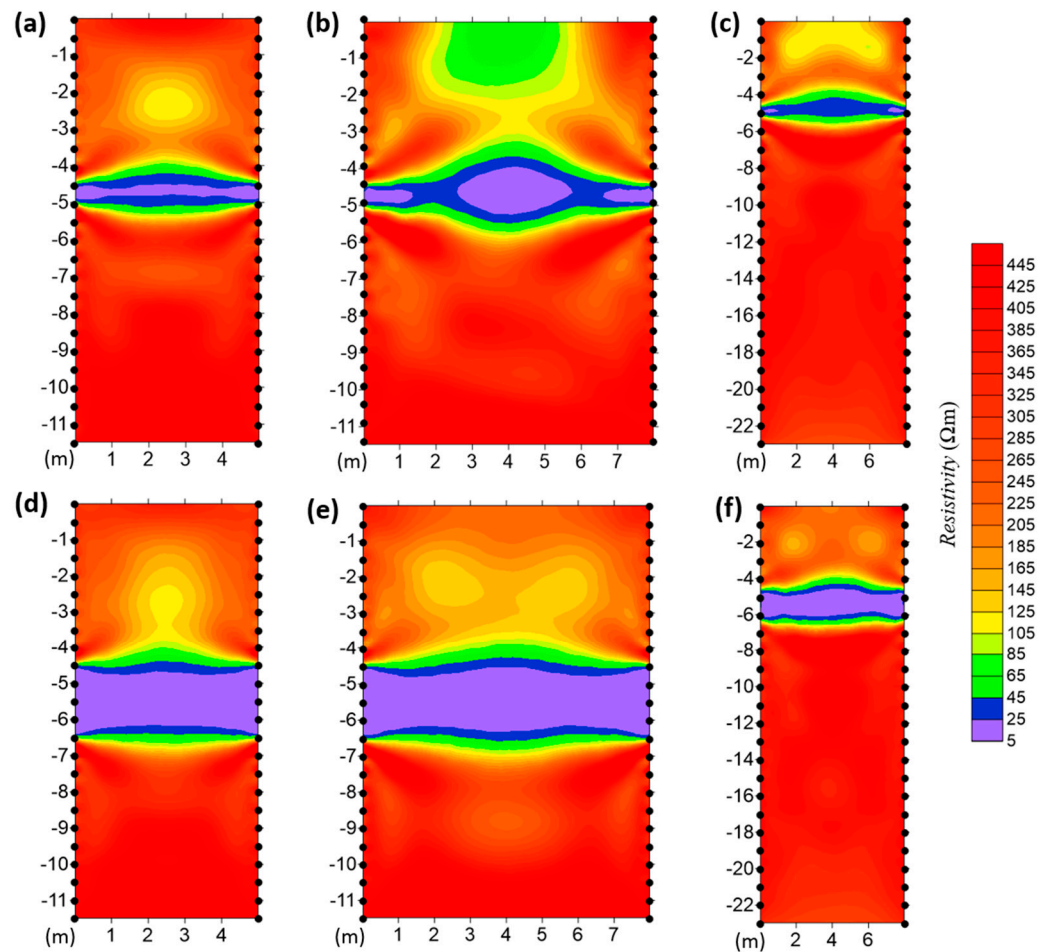


Figure 7. (a) shows the inverted synthetic model of Figure 3a; (b) shows the inverted synthetic model of Figure 3b; (c) shows the inverted synthetic model of Figure 3c; (d) shows the inverted synthetic model of Figure 3d; (e) shows the inverted synthetic model of Figure 3e; (f) shows the inverted synthetic model of Figure 3f.

4.2. ERT Field Data Inversion

Figure 8 shows the inverted resistivity model obtained from the ERT surface measurements performed upstream of the contaminated area and in correspondence with the line where the trench was subsequently excavated. In the shallow portion of the image, a high-resistivity layer ($\rho > 2000 \Omega\text{m}$) corresponds to an unsaturated gravel layer. At about a 7 m depth, a sharp resistivity variation is found ($\rho < 200 \Omega\text{m}$), corresponding to the contact with the clay layer. In the right part ($x > 50 \text{ m}$), this boundary is deeper, and the high-resistivity layer reaches a depth of about 10 m. Finally, the clay layer seems to extend to the bottom of the section along the entire measured transect. However, as discussed above for synthetic modelling, this is only an indication of the continuity of the clay layer, and is not to any extent an evaluation of its thickness. In fact, $200 \Omega\text{m}$ is a value far too high for the resistivity of clay: this testifies to the emergence of an example of the equivalence problem. In fact, the clay layer is much thinner and much more conductive.

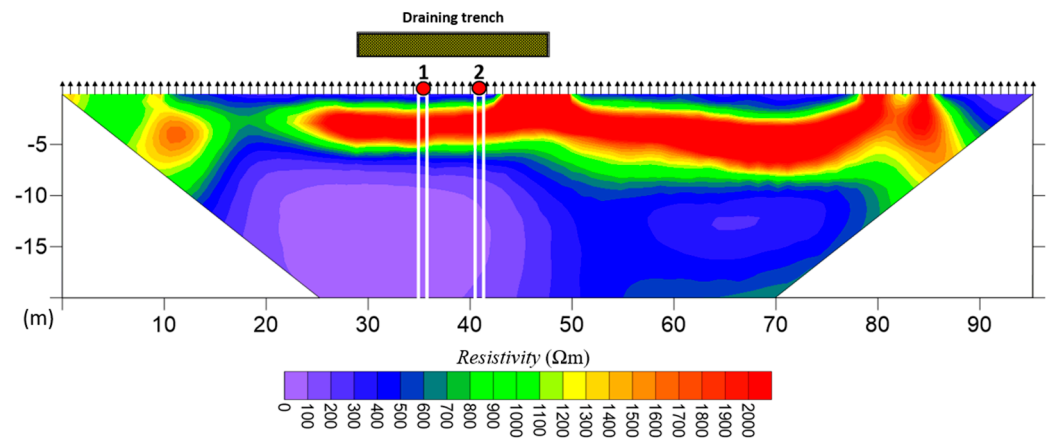


Figure 8. Inverted resistivity model of the surface ERT survey line collected upstream of the contaminated area. Based on this result, the draining trench (brownish rectangle) and the boreholes (red dots and white polygons) were realized approximately in the middle of the transect.

Figure 9 presents the inverted resistivity models obtained with the measurements performed using the ERT cross-borehole configuration before the trench excavation. The measurements were collected across boreholes 1–2 (Figure 9a), boreholes 1–3 (Figure 9b), and boreholes 2–4 (Figure 9c). All models show practically the same subsurface structure: an upper high-resistivity layer ($\rho \approx 1000 \Omega\text{m}$), i.e., a gravel layer, a low-resistivity layer ($\rho < 10 \Omega\text{m}$), i.e., a clay layer at a 6–7 m depth with a thickness of about 0.50 m, and a deeper high-resistivity layer of gravel.

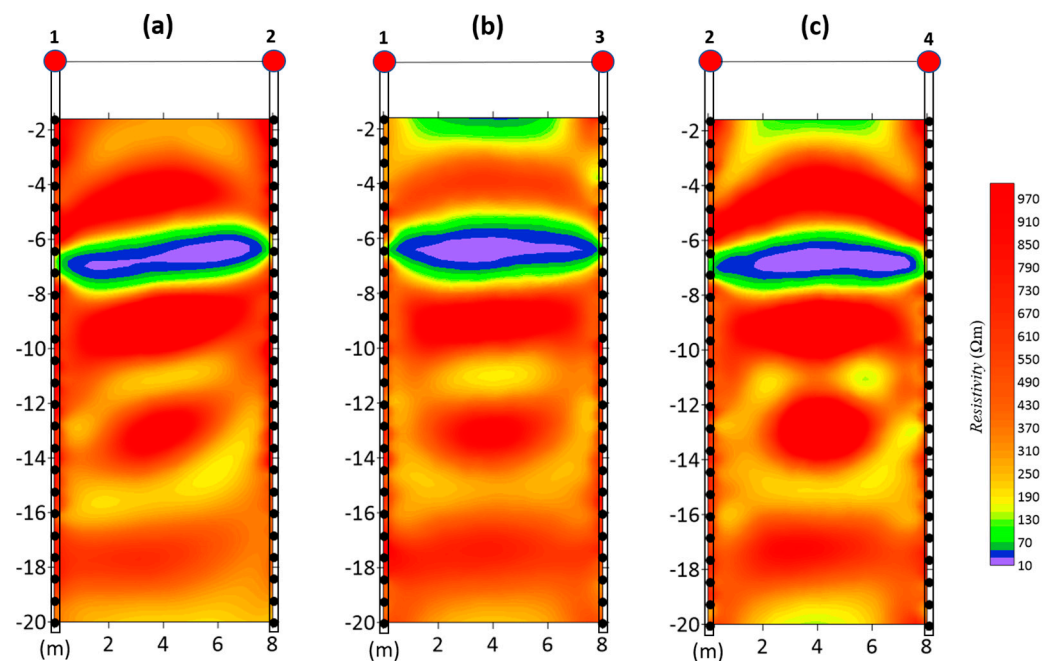


Figure 9. Inverted resistivity models of the cross-borehole (red dots) ERT surveys: (a) model between borehole 1 and 2; (b) model between borehole 1 and 3; (c) model between borehole 2 and 4.

Figure 10a shows the result of the time-lapse ratio inversion applied to the ERT cross-borehole measurements in the boreholes 1–3 section, acquired before and after the excavation of the trench. On the other hand, Figure 10b presents the result of the time-lapse ratio inversion applied to the same ERT cross-borehole datasets (boreholes 1–3), both collected after the realization of the trench (one month apart).

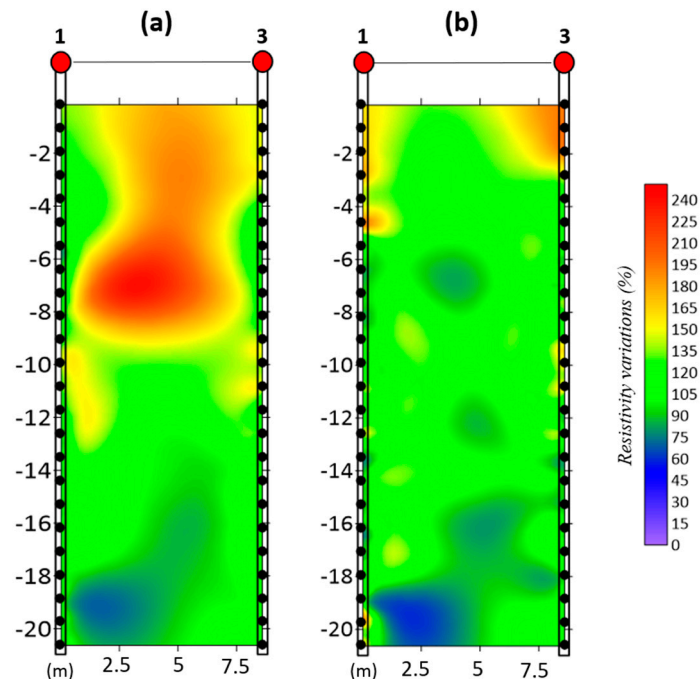


Figure 10. (a) ERT cross-borehole (boreholes 1–3) ratio inversion result: first dataset was collected before the realization of the draining trench and the second one collected after the realization; (b) ERT cross-borehole (boreholes 1–3) ratio inversion result of two datasets, both collected after the realization of the draining trench.

From the results shown in Figure 10a, the effect of the excavation is clear, with an increase in the resistivity of the central area of the section down to a 9–10 m depth, corresponding to the depth of the trench, interrupting the continuity of the clay layer. The material used to fill the trench (permeable coarse gravel) most likely has a very similar electrical resistivity to the lowermost gravel layer; for this reason, no great resistivity variations are detected below 9 m. This result is confirmed by the model in Figure 10b, which does not show high apparent variations in resistivity in the post-excavation inverted models.

4.3. ERT Time-Lapse Inversions during Water Infiltration Experiments

Figure 11 shows the results of the time-lapse cross-hole ERT monitoring of the first infiltration experiment monitored with ERT time-lapse cross-borehole measurements (along the profile of boreholes 1–2).

It is clear that, during the entire experiment, resistivity variations do not affect the at 6–7 m-deep clay layer (white dashed line in the panels of Figure 11, derived from the evidence from Figure 9a), and it is therefore not directly crossed by the water flow along this profile. This is consistent with the fact that along the borehole 1–2 profile, the clay layer is not cut by the trench. The shallow part of the subsurface above the clay layer is clearly affected by the water infiltration (Figure 11a–e). Afterward, in Figure 11f, evidence suggests that the water flow propagates deeper, possibly as an effect of water getting into the nearby, off-section trench and finding its way to the deeper gravels. These negative resistivity variations increase until water is injected (Figure 11g), but once the irrigation is stopped, a progressive decrease in this effect is observed in the subsequent time steps (Figure 11h–k), and the overall infiltration effect slowly fades away until the last measurement (Figure 11l).

Figure 12 shows the result of the second infiltration experiment monitored via ERT time-lapse cross-borehole measurements using the cross-hole configuration of boreholes 2–4.

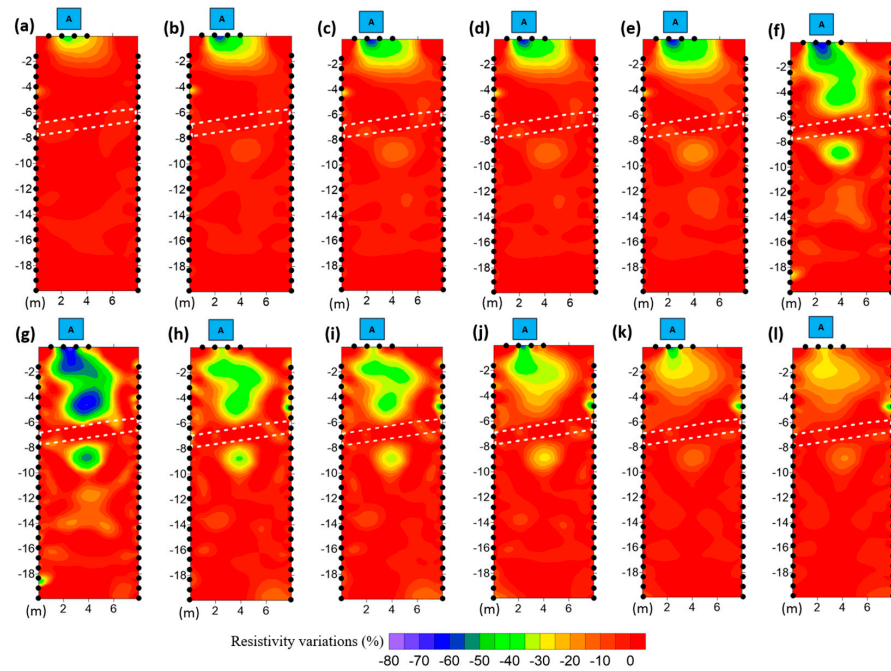


Figure 11. Cross-hole time-lapse ERT results corresponding to infiltration experiment 1. The injection point (blue square A) is located between boreholes 1 and 2; the same used for the ERT cross-hole acquisition. The white dashed line represents the clay layer detected in the inverted resistivity model of Figure 9a—note that along this profile, the clay layer is NOT interrupted by the trench (see Figure 2b). (a–l) represent, respectively, the results of the time-lapse ratio inversion applied at time steps t1–t12 presented in Table 1 using dataset t0 as the reference data.

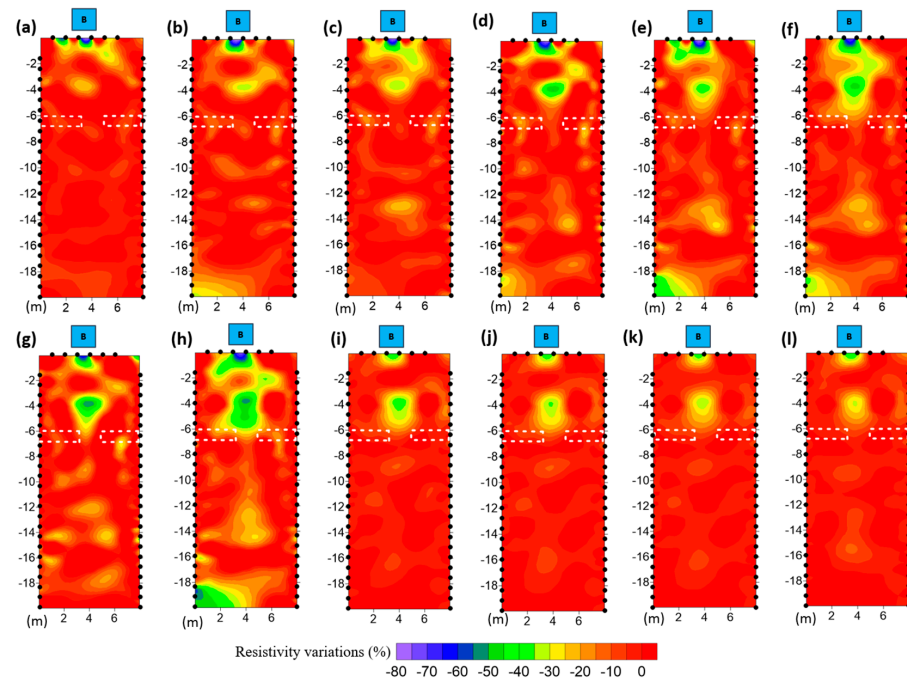


Figure 12. Cross-hole time-lapse ERT results corresponding to infiltration experiment 2. The injection point (blue square B) is located between boreholes 2 and 4; the same used for ERT acquisition. The white dashed line represents the clay layer detected in the inverted resistivity model of Figure 9c, which is cut in the middle with a discontinuity of 1 m representing the draining trench. (a–l) represent the results of the ERT time-lapse ratio inversion applied at time steps t1–t12 presented in Table 1 using dataset t0 as the reference data.

In this case, the clay layer at 6–7 m depth is discontinuous as an effect of trench digging along the monitoring section (boreholes 2–4) and the water infiltration point is right on the vertical of the trench in the middle of the section itself. Once the water injection begins, clear negative resistivity variations propagate vertically (Figure 12a–e) and cross the discontinuity of the clay layer (Figure 12f–h), albeit losing intensity possibly because of lateral spread, as detected in the companion results of the first infiltration experiment (Figure 11). Note that the colour scale in Figure 12 highlights considerable negative variations in resistivity, and the changes in resistivity across the trench (e.g., in Figure 12h) are substantial, reaching a depth of about 16 m, where infiltration seems to stop. As in the first infiltration experiment, once infiltration ceases from the surface, a progressive decrease in the negative resistivity variation signal takes place (Figure 12i,j), and is practically null in the latest measurements (Figure 12k,l).

4.4. GPR Monitoring during Water Infiltration Experiments

We also conducted cross-hole GPR monitoring during the second infiltration test. In order to efficiently follow the infiltration process, we planned to use the same step of the time-lapse ERT. Thus, we collected both ZOP surveys and more detailed MOG data. In the following, we will only present the more effective MOG results. These were acquired with a vertical spacing between the antenna positions equal to 0.5 m for the entire length of both boreholes 2 and 4.

The results are shown in Figure 13, where both the initial and final (AM and PM in Figure 13) instants are shown. The data were inverted using the PRONTO inversion code [36]. Travel-time data (Figure 13a,d) were thus inverted into GPR velocity distributions (Figure 13b,e), and these in turn into estimations of moisture content (Figure 13c,f) using the relationship presented by Topp et al. (1980) [37]. While subtle differences in moisture content are visible in the 2D images, more readable results are obtained by averaging the results along horizontal lines, thus producing 1D vertical profiles (Figure 13g). It is clear that there is a substantial overall increase in moisture content across the profile—with a strong peak corresponding to the wet clay layer—extending to a maximum depth of 16 m, consistent with the time-lapse ERT evidence (Figure 12).

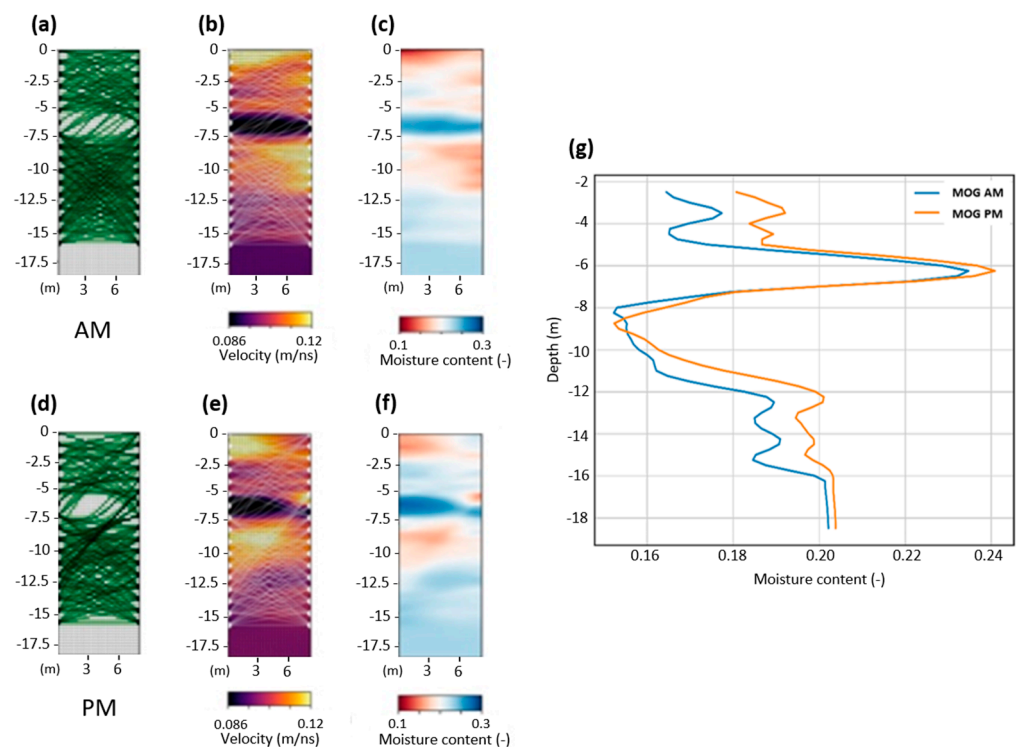


Figure 13. Cross-hole time-lapse GPR results corresponding to infiltration experiment 2.

5. Discussion

The obtained results demonstrate that advanced geophysical applications can be fundamental tools to improve the characterization of a contaminated site, both in terms of its structure and fluid dynamics. In particular, ERT and GPR cross-borehole surveys in time-lapse configuration can be efficiently integrated to monitor and understand local infiltration dynamics.

In this specific context, the existence of a highly conductive layer of clay at a 5 m depth poses a severe challenge to surface ERT investigations. Forward modelling shows that short transects and low dipole skips do not allow us to define the correct structure of the subsoil (Figures 4a–c and 5a–c). Increasing the length of the electrode array and the dipole skip leads to slightly better inverted models, but the thickness of the clay layer is still much larger than expected (Figures 4d and 5d). Inverted synthetic models with clay layers with thicknesses of 0.5 m (Figure 4d) and 2 m (Figure 5d) are quite similar and it is difficult to discriminate between them. This problem is further emphasized by increasing the depth of the clay layer to 10 m (Figure 6), which would require longer transects to be correctly detected. The inversion results of the field datasets confirm the limits of the surface ERT surveys to define a subsoil structure with a clay level between high-resistive gravel layers, as expected from the well-known equivalence problem. Although, in reality, the dataset was acquired with an electrode array of 96 m and with a dipole–dipole skip 8 configuration, in the inverted resistivity model obtained upstream of the contaminated site (Figure 8), it is possible to correctly define the depth of the clay layer (6–7 m) but not its thickness, which is clearly amplified till the bottom. This is probably due to a short-circuiting problem in the subsoil, as the electric current tends to flow in the less resistive layer of clay instead of propagating into the underlying resistive gravel layer.

On the contrary, forward modelling using cross-borehole configurations demonstrates that this method can define the real subsurface structure, i.e., the depth, thicknesses and resistivity values of each layer. However, the geometry of the boreholes (distance and depth), and the spacing of the electrodes must be adequately designed. The distance between boreholes should not be larger than half the length of the electrode array in the borehole [15]. Larger separations lead to a significant decrease in sensitivity at the centre of the model and the probable development of unrealistic artefacts, e.g., Figure 7b,c. The spacing of electrodes also affects the quality of the inverted models; i.e., with a spacing lower than the thickness of the layers, it is possible to precisely define their depth, thickness, and resistivity values (e.g., Figure 7a,d). The results of forward modelling are confirmed by the results obtained with the field datasets, and the corresponding inverted models (Figure 9) show the same subsurface structure found in borehole cores.

The results obtained from the cross-borehole ERT measurements, performed to verify the effect of draining trench excavation, demonstrate the reliability of the ratio inversion approach. The excavation, filled with coarse and permeable granular sediment, is clearly apparent in the inverted ERT results in Figure 10a (obtained by comparing pre-trench and post-trench ERT datasets), with an increase in resistivity developing from the surface down to a 8–9 m depth, thus interrupting the continuity of the clay layer.

Finally, the infiltration experiments with cross-borehole ERT measurements in time-lapse configuration verify the effectiveness of the draining trench. Even when injecting the water in a lateral position with respect to the trench, such as in the first experiment (Figure 11), the water is drained below the clay layer and 18 h after the end of the injection (t_{12}), the subsoil has practically returned to the initial natural conditions (t_0). In the second infiltration experiment (Figure 12), carried out right above the trench, after the beginning of the experiment, the water infiltrated more quickly depth-wise compared to the first experiment (compare the negative resistivity variations in Figures 11a–e and 12a–e), and the flow crosses the discontinuity of the clay layer, as shown in Figure 12f–h. Once the water injection is completed, the conditions return more quickly to the initial natural conditions (t_0) compared to the first experiment (compare the negative resistivity variations in Figures 11i–l and 12i–l), as expected considering that the injection position was exactly

above the trench. Therefore, the results of these two experiments confirm that the trench is correctly draining the sub-surface water flow into the deeper gravel layer, thus preventing it from reaching the critical contaminated area.

The GPR data, and particularly the high-resolution MOG data (Figure 13), fully confirm the evidence from ERT, in particular the fast infiltration of the injected water above the trench and its resting on top of a further discontinuity at about a depth of 16 m.

6. Conclusions

The obtained results demonstrate that geophysical investigations are a valuable tool for the characterization of contaminated sites and for the management of remediation and secure strategies. In relatively short times and with limited costs, it is possible to obtain additional and more extensive information compared to direct investigations, e.g., variations in depths and thicknesses and discontinuities in the layers in the subsoil.

The use of preliminary information from the investigation site to perform a forward modelling process is an excellent strategy to properly define the acquisition parameters of ERT field measurements, i.e., the array length, electrode spacing, acquisition scheme, and borehole separation.

In environments with very conductive layers interspersed between more resistive layers, it is necessary to pay particular attention to the interpretation of results derived from surface ERT measurements, particularly in the evaluation of the thicknesses and depths of the layers. As apparent from the obtained results in this case study, both from synthetic datasets and field datasets, it is not possible to correctly define the real thickness of the clay layer, which seems to extend deeper in the inverted models. However, this is an important indication of the continuity of such a layer that has key implications for the water subsurface circulation at the site. However, to define the correct structure of the subsurface, it is necessary to perform ERT survey in cross-hole configuration, using appropriate borehole and electrode geometries, i.e., borehole length and separation and electrode spacing, and acquisition schemes.

The ratio inversion applied to ERT time-lapse surveys is a reliable approach for verifying natural or induced variations in the subsoil, which would be difficult to identify by comparing the resistivity models obtained by individual inversions. At the investigated site, the resistivity variation results (Figures 10–12) allow for an easy evaluation of the effect of the excavation of the trench and its effectiveness in draining the sub-surface water flow in the deeper gravel layer.

Cross-hole GPR is also a powerful technique, and in this case fully corroborates the ERT results, pointing more directly towards a quantitative estimation of moisture content and its space–time changes.

Author Contributions: Conceptualization, G.C.; methodology, G.C.; validation, G.C.; formal analysis, M.P. and B.M.; investigation, G.C., J.B., L.P., I.B., B.M. and G.C.; resources, G.C.; data curation, M.P. and B.M.; writing—original draft preparation, M.P.; writing—review and editing, G.C., J.B., L.P., I.B. and B.M.; visualization, M.P., J.B. and G.C.; supervision, G.C.; project administration, G.C.; funding acquisition, G.C. All authors have read and agreed to the published version of the manuscript.

Funding: This study was carried out within the RETURN Extended Partnership and received funding from the European Union Next-Generation EU (National Recovery and Resilience Plan—NRRP, Mission 4, Component 2, Investment 1.3—D.D. 1243 2/8/2022, PE0000005).

Data Availability Statement: Datasets used in this research will be sent to interested researchers upon request.

Acknowledgments: The authors acknowledge that this work is based on the thesis of Mirko Pavoni—Department of Geosciences—University of Padova.

Conflicts of Interest: The authors declare no conflicts of interest.

References

1. Cassiani, G.; Binley, A.; Kemna, A.; Wehrer, M.; Orozco, A.F.; Deiana, R.; Boaga, J.; Rossi, M.; Dietrich, P.; Werban, U.; et al. Noninvasive Characterization of the Trecate (Italy) Crude-Oil Contaminated Site: Links between Contamination and Geophysical Signals. *Environ. Sci. Pollut. Res.* **2014**, *21*, 8914–8931. [[CrossRef](#)] [[PubMed](#)]
2. Binley, A.; Hubbard, S.S.; Huisman, J.A.; Revil, A.; Robinson, D.A.; Singha, K.; Slater, L.D. The Emergence of Hydrogeophysics for Improved Understanding of Subsurface Processes over Multiple Scales. *Water Resour. Res.* **2015**, *51*, 3837–3866. [[CrossRef](#)]
3. Wang, T.P.; Chen, C.C.; Tong, L.T.; Chang, P.Y.; Chen, Y.C.; Dong, T.H.; Cheng, S.N. Applying FDEM, ERT and GPR at a site with soil contamination: A case study. *J. Appl. Geophys.* **2015**, *121*, 21–30. [[CrossRef](#)]
4. Godio, A.; Arato, A.; Stocco, S. Geophysical Characterization of a Nonaqueous-Phase Liquid-Contaminated Site. *Environ. Geosci.* **2010**, *17*, 141–161. [[CrossRef](#)]
5. Binley, A. Tools and Techniques: Electrical Methods. In *Treatise on Geophysics*; Elsevier: Amsterdam, The Netherlands, 2015; pp. 233–259.
6. Doetsch, J.; Linde, N.; Pessognelli, M.; Green, A.G.; Günther, T. Constraining 3-D Electrical Resistance Tomography with GPR Reflection Data for Improved Aquifer Characterization. *J. Appl. Geophys.* **2012**, *78*, 68–76. [[CrossRef](#)]
7. Santi, P.M.; McCray, J.E.; Martens, J.L. Investigating Cross-Contamination of Aquifers. *Hydrogeol. J.* **2006**, *14*, 51–68. [[CrossRef](#)]
8. Doetsch, J.; Linde, N.; Binley, A. Structural Joint Inversion of Time-lapse Crosshole ERT and GPR Traveltime Data. *Geophys. Res. Lett.* **2010**, *37*. [[CrossRef](#)]
9. Deiana, R.; Cassiani, G.; Kemna, A.; Villa, A.; Bruno, V.; Bagliani, A. An Experiment of Non-invasive Characterization of the Vadose Zone via Water Injection and Cross-hole Time-lapse Geophysical Monitoring. *Near Surf. Geophys.* **2007**, *5*, 183–194. [[CrossRef](#)]
10. Steelman, C.M.; Klazinga, D.R.; Cahill, A.G.; Endres, A.L.; Parker, B.L. Monitoring the evolution and migration of a methane gas plume in an unconfined sandy aquifer using time-lapse GPR and ERT. *J. Contam. Hydrol.* **2017**, *205*, 12–24. [[CrossRef](#)]
11. Fontana, A.; Mozzi, P.; Marchetti, M. Alluvial Fans and Megafans along the Southern Side of the Alps. *Sediment. Geol.* **2014**, *301*, 150–171. [[CrossRef](#)]
12. Fontana, A.; Mozzi, P.; Bondesan, A. Alluvial Megafans in the Venetian–Friulian Plain (North-Eastern Italy): Evidence of Sedimentary and Erosive Phases during Late Pleistocene and Holocene. *Quat. Int.* **2008**, *189*, 71–90. [[CrossRef](#)]
13. Hippe, K.; Fontana, A.; Hajdas, I.; Ivy-Ochs, S. A High-Resolution ¹⁴C Chronology Tracks Pulses of Aggradation of Glaciofluvial Sediment on the Cormor Megafan between 45 and 20 Ka BP. *Radiocarbon* **2018**, *60*, 857–874. [[CrossRef](#)]
14. Fontana, A.; Rossato, S.; Poli, M.E.; Furlani, S.; Stefani, C. *Carta delle Unità Geologiche della Pianura del Friuli Venezia Giulia: Scala 1:150.000*; Università degli Studi di Trieste: Trieste, Italy, 2019; ISBN 9788894039429.
15. Binley, A.; Kemna, A. DC Resistivity and Induced Polarization Methods. In *Hydrogeophysics*; Rubin, Y., Hubbard, S.S., Eds.; Springer: Dordrecht, The Netherlands, 2005; pp. 129–156.
16. Blanchy, G.; Saneiyani, S.; Boyd, J.; McLachlan, P.; Binley, A. ResIPy, an Intuitive Open Source Software for Complex Geoelectrical Inversion/Modeling. *Comput. Geosci.* **2020**, *137*, 104423. [[CrossRef](#)]
17. Wagner, F.M.; Uhlemann, S. An Overview of Multimethod Imaging Approaches in Environmental Geophysics. In *Advances in Geophysics*; Elsevier: Amsterdam, The Netherlands, 2021; pp. 1–72.
18. Constable, S.C.; Parker, R.L.; Constable, C.G. Occam’s Inversion: A Practical Algorithm for Generating Smooth Models from Electromagnetic Sounding Data. *Geophysics* **1987**, *52*, 289–300. [[CrossRef](#)]
19. Slater, L.; Binley, A. Synthetic and Field-Based Electrical Imaging of a Zerovalent Iron Barrier: Implications for Monitoring Long-Term Barrier Performance. *Geophysics* **2006**, *71*, B129–B137. [[CrossRef](#)]
20. Pavoni, M.; Carrera, A.; Boaga, J. Improving the Galvanic Contact Resistance for Geoelectrical Measurements in Debris Areas: A Case Study. *Near Surf. Geophys.* **2022**, *20*, 178–191. [[CrossRef](#)]
21. Pavoni, M.; Boaga, J.; Carrera, A.; Zuecco, G.; Carturan, L.; Zumiani, M. Brief Communication: Mountain Permafrost Acts as an Aquitard during an Infiltration Experiment Monitored with Electrical Resistivity Tomography Time-Lapse Measurements. *Cryosphere* **2023**, *17*, 1601–1607. [[CrossRef](#)]
22. Pavoni, M.; Boaga, J.; Wagner, F.M.; Bast, A.; Phillips, M. Characterization of Rock Glaciers Environments Combining Structurally-Coupled and Petrophysically-Coupled Joint Inversions of Electrical Resistivity and Seismic Refraction Datasets. *J. Appl. Geophys.* **2023**, *215*, 105097. [[CrossRef](#)]
23. Nielson, T.; Bradford, J.; Pierce, J.; Seyfried, M. Soil Structure and Soil Moisture Dynamics Inferred from Time-Lapse Electrical Resistivity Tomography. *Catena* **2021**, *207*, 105553. [[CrossRef](#)]
24. Lapenna, V.; Perrone, A. Time-Lapse Electrical Resistivity Tomography (TL-ERT) for Landslide Monitoring: Recent Advances and Future Directions. *Appl. Sci.* **2022**, *12*, 1425. [[CrossRef](#)]
25. Doetsch, J.; Linde, N.; Vogt, T.; Binley, A.; Green, A.G. Imaging and quantifying salt-tracer transport in a riparian groundwater system by means of 3D ERT monitoring. *Geophysics* **2012**, *77*, B207–B218. [[CrossRef](#)]
26. Daily, W.; Ramirez, A.; LaBrecque, D.; Nitao, J. Electrical Resistivity Tomography of Vadose Water Movement. *Water Resour. Res.* **1992**, *28*, 1429–1442. [[CrossRef](#)]
27. Topp, G.C.; Davis, J.L. Measurement of Soil Water Content Using Time-domain Reflectometry (TDR): A Field Evaluation. *Soil Sci. Soc. Am. J.* **1985**, *49*, 19–24. [[CrossRef](#)]

28. Roth, K.; Schulin, R.; Flühler, H.; Attinger, W. Calibration of Time Domain Reflectometry for Water Content Measurement Using a Composite Dielectric Approach. *Water Resour. Res.* **1990**, *26*, 2267–2273. [[CrossRef](#)]
29. van Overmeeren, R.A.; Sariowan, S.V.; Gehrels, J.C. Ground Penetrating Radar for Determining Volumetric Soil Water Content; Results of Comparative Measurements at Two Test Sites. *J. Hydrol.* **1997**, *197*, 316–338. [[CrossRef](#)]
30. Robinson, D.A.; Friedman, S.P. A Method for Measuring the Solid Particle Permittivity or Electrical Conductivity of Rocks, Sediments, and Granular Materials. *J. Geophys. Res. Solid Earth* **2003**, *108*. [[CrossRef](#)]
31. Rossi, M.; Cassiani, G.; Binley, A. A Stochastic Analysis of Cross-Hole Ground-Penetrating Radar Zero-Offset Profiles for Subsurface Characterization. *Vadose Zone J.* **2012**, *11*, vzt2011-0078. [[CrossRef](#)]
32. Parkin, G.; Redman, D.; Von Bertoldi, P.; Zhang, Z. Measurement of soil water content below a wastewater trench using ground-penetrating radar. *Water Resour. Res.* **2000**, *36*, 2147–2154. [[CrossRef](#)]
33. Deiana, R.; Cassiani, G.; Villa, A.; Bagliani, A.; Bruno, V. Calibration of a Vadose Zone Model Using Water Injection Monitored by GPR and Electrical Resistance Tomography. *Vadose Zone J.* **2008**, *7*, 215–226. [[CrossRef](#)]
34. Pringle, J.K.; Westerman, A.R.; Clark, J.D.; Guest, J.A.; Ferguson, R.J.; Gardiner, A.R. The use of vertical radar profiling (VRP) in GPR surveys of ancient sedimentary strata. In *Ground Penetrating Radar in Sediments*; Geological Society: London, UK, 2003; Volume 211, pp. 225–246. [[CrossRef](#)]
35. Doetsch, J.A.; Coscia, I.; Greenhalgh, S.; Linde, N.; Green, A.; Günther, T. The Borehole-Fluid Effect in Electrical Resistivity Imaging. *Geophysics* **2010**, *75*, F107–F114. [[CrossRef](#)]
36. LaBrecque, D.; Alumbaugh, D.L.; Yang, X.; Paprocki, L.; Brainard, J. Chapter 15 Three-Dimensional Monitoring of Vadose Zone Infiltration Using Electrical Resistivity Tomography and Cross-Borehole Ground-Penetrating Radar. In *Methods in Geochemistry and Geophysics*; Elsevier: Amsterdam, The Netherlands, 2002; pp. 259–272.
37. Topp, G.C.; Davis, J.L.; Annan, A.P. Electromagnetic Determination of Soil Water Content: Measurements in Coaxial Transmission Lines. *Water Resour. Res.* **1980**, *16*, 574–582. [[CrossRef](#)]

Disclaimer/Publisher’s Note: The statements, opinions and data contained in all publications are solely those of the individual author(s) and contributor(s) and not of MDPI and/or the editor(s). MDPI and/or the editor(s) disclaim responsibility for any injury to people or property resulting from any ideas, methods, instructions or products referred to in the content.